Numerical and optical soot characterization through 2-color pyrometry technique for an innovative diesel piston bowl design

Fuel 333 (2023) 126347

Contents lists available at ScienceDirect

Fuel

journal homepage: www.elsevier.com/locate/fuel

Full Length Article

Numerical and optical soot characterization through 2-color pyrometry technique for an innovative diesel piston bowl design

A. Piano [a,*], S. Roggio [a], F. Millo [a], A. García [b], C. Micó [b], F. Lewiski [b], F.C. Pesce [c], A. Vassallo [c], A. Bianco [d]

[a] Politecnico di Torino, Italy
[b] CMT – Motores Térmicos, Universitat Politècnica de València, Spain
[c] PUNCH Torino S.p.A/ Formerly General Motors Global Propulsion Systems, Italy
[d] Powertech Engineering Srl, Italy

ARTICLE INFO

Keywords:
Innovative diesel engine piston bowl
Optical engine
2-Color pyrometry technique
Computational Fluid Dynamics
Numerical optical soot density KL

ABSTRACT

The development of innovative diesel piston bowl designs has shown significant improvement of the near-wall flame evolution, resulting in lower fuel consumption and engine-out soot emissions. With this aim, a novel hybrid piston bowl for a 1.6 L light-duty diesel engine was designed, coupling a sharp-stepped bowl and radial-bumps in the inner bowl rim. The effects of the proposed hybrid bowl were analysed through both single-cylinder optical engine and 3D-CFD models, which feature a detailed chemical kinetic mechanism and the Particulate Mimic (PM) soot model. The 2-color pyrometry optical technique was adopted to obtain the optical soot density (KL) and the temperature of the soot surface. Then, a line-of-sight integration of the numerical soot distribution was adopted to obtain a planar KL distribution, which is directly comparable with the experimental KL images. The results showed a good agreement in terms of soot distribution between 3D-CFD and experiments, confirming the high prediction capabilities of the developed numerical methodology. The synergetic application of numerical and optical techniques highlighted that the hybrid bowl strongly mitigates the flame-to-flame interaction with respect to a conventional re-entrant bowl, leading to lower soot formation in the flame collision area. Moreover, faster flame propagation toward the cylinder axis is highlighted with a consequent higher soot oxidation rate in the late combustion phase.

1. Introduction

The transport sector needs to face the challenge of reducing pollutant as well as CO_2 emissions to ensure a sustainable future. A variety of new technologies and propulsion systems have been proposed to achieve this objective. The electrification and hybridization are two of the most attractive alternatives that have been considered as potential solution for replacing the Internal Combustion Engines (ICE) [1]. It is true that the future of the light-duty transport seems to go toward this direction. However, for the medium and heavy-duty applications mostly powered by diesel engines, the massive electrification in a near-medium term is not clear. The weight of batteries, the autonomy provided by liquid fuels, the costs and the lack of infrastructure among other reasons, suggest that in this sector the ICE will still play an important role. Therefore, manufacturers and research groups are still investing on the development of new technologies (based on alternative combustion modes or new hardware design) [2–5] and fuels [6–8] which will help achieving the emissions targets.

Focusing on new hardware development for compression ignition engines (CI), the use of innovative piston geometries has demonstrated to be a very effective solution for reducing the well-known NO_X-soot trade-off [9,10]. The piston geometry defines the wall-spray interaction, which affects the fuel–air mixture process and consequently, the flame movement inside the combustion chamber. Several authors have demonstrated the potential of innovative designs in improving the soot late cycle oxidation, thus allowing to use high EGR rates [11,12] to further reduce NO_X formation without increasing soot emissions. Among different proposals, it is worth highlighting those based on the inclusion of a chamfered lip, which is located at the top edge of the bowl and replaces the typical protruding lip present in the more conventional so-called re-entrant pistons. This concept, known as “stepped lip”, is designed to split the spray in two parts, redirecting one of them downward within the bowl and the other one towards the squish zone [13],

* Corresponding author.
E-mail address: andrea.piano@polito.it (A. Piano).

https://doi.org/10.1016/j.fuel.2022.126347
Received 30 June 2022; Received in revised form 2 September 2022; Accepted 12 October 2022

Abbreviations

AMR	Adaptive Mesh Refinement
CAD aTDC	Crank Angle Degrees after Top Dead Center
CFD	Computational Fluid Dynamics
CI	Compression Ignition
EGR	Exhaust Gas Recirculation
ICE	Internal Combustion Engine
IMEP	Indicated Mean Effective Pressure
IVC	Intake Valve Closure
KH-RT	Kelvin Helmholtz and Rayleigh Taylor
KL	Optical soot density
L	LOS path length
LOS	Line-of-sight
NTC	No Time Counter
PAH	Poly-cyclic Aromatic Hydrocarbons
PM	Particulate Mimic
RANS	Reynolds-averaged Navier-Stokes
RNG	Re-Normalization Group
TDC	Top Dead Center
VGT	Variable Geometry Turbine
2C	2-color pyrometry technique
λ	Wavelength
$I_{b,\lambda}$	Monochromatic intensity of radiation of a black body
I_λ	Monochromatic intensity of radiation
ε_λ	Monochromatic soot emissivity
$T_{a,\lambda}$	Monochromatic apparent temperature
f_v	Soot volume fraction
τ_λ	Monochromatic soot transmissivity
ρ_{wall}	Wall reflectivity

improving the air utilization and air–fuel mixing in the whole combustion chamber. The implementation of this concept provides a significant reduction of soot [14–16] as well as a shorter combustion duration in comparison with the re-entrant piston [12,17]. In 2016, Mercedes-Benz launched a new family of engines named OM654, where the pistons were designed including the stepped lip geometry. The company reported an important reduction of particulate emissions and fuel consumption [18].

A different approach was recently proposed by the Volvo Group, with the aim of reducing the engine out soot emissions. This concept consists of the introduction of radial protrusions (radial bumps) around the piston bowl circumference. The aim is to drive the flames towards the bowl centre after reaching the bowl periphery. In this way, the flame could reach zones of the combustion chamber around the injector where fresh oxygen is still available. In addition, this movement avoids the flames to spread tangentially, reducing the flame-to-flame collision and the formation of fuel rich zones [19], where soot is formed. Volvo reported a significant reduction of soot emissions (around 80 %) as well as a faster burn out [20], opening a door to achieve soot reductions without penalizing the NO_X emissions (NO_X-soot trade-off reduction). Recently, a similar piston bowl design for a light-duty diesel engine was numerically assessed in [21]. In this work, the radial bumps led to an improvement of the air/fuel mixing with respect to a conventional re-entrant bowl. Under partial load engine operating condition, a flatness in the trade-offs were observed, resulting in 50 % soot and 5 % Brake Specific Fuel Consumption (BSFC) reduction with respect to the re-entrant bowl.

More recent studies propose the combination of the stepped lip and the radial protrusions as a further step towards the ultra-low soot emission pistons concept [22]. Experimental tests, both in single cylinder optical and metal engines, using this design have demonstrated an impressive soot reduction [23,24] and a shorter combustion duration (due to the faster late-cycle oxidation [25]) in comparison with more conventional re-entrant designs. Moreover, recent studies have been able to characterize the effect of this novel geometry over in-cylinder air–fuel mixing and flame propagation [26], which are strongly linked with the soot formation reduction achieved. However, this concept is at an early stage of development and there is still room for improvement. In this scenario, tools like 3D-Computational Fluid Dynamics (3D-CFD) simulations are of great interest to deepen in the behaviour of these novel piston geometries thanks to its high predictive capabilities and reduced costs compared to experimental campaigns.

Considering all the above mentioned, the aim of the current work is to characterize the soot formation and oxidation processes, influenced by an innovative piston design. Similarly to the piston bowl designed in [24], it exploits both stepped lip and the radial bumps concepts to maximize in-cylinder soot reduction. For this purpose, the work proposes a synergetic combination of both 3D-CFD and experimental measurements in an optical engine. The numerical study was carried out following the same procedure described in [27] using 1D-CFD models to obtain reliable calculations of the injection rate and boundary conditions to initialize the 3D-CFD simulations. The numerical soot data has been compared with 2-colour pyrometry KL experimental measurements, obtained from an optical engine based on the same platform. For this purpose, two different approaches have been proposed and evaluated: one based on the integration of the numerical soot volume fraction along the optical path length; the other based on an equivalent KL parameter, calculated from the numerical soot volume fraction. It must be considered that just a qualitative comparison between 3D-CFD and experimental data was performed due to intrinsic differences in terms of layout (i.e., metal engine vs optical engine). More details in this regard can be found in [26]. The numerical results, in agreement with the experiments, confirm the effect of the radial protrusions over the flame dynamics and the soot formation. Besides, the comparison highlights the agreement between the numerical soot volume fraction and the experimental KL, which could be considered as a reference for future comparisons.

2. Simulation methodology

2.1. Test engine

The numerical analysis was carried out considering as a test case a 4-cylinder 1.6 L light-duty diesel engine, featuring a common rail injection system with a latest generation 8-hole solenoid injector. The main features of the test engine are summarized in Table 1.

Two different combustion systems were analysed: the baseline design is a conventional re-entrant bowl, as shown in Fig. 1 – left. Then, an innovative piston bowl is proposed, named 'hybrid' hereafter. It features an annular recess step and a number of radial bumps in the inner bowl rim equal to the number of injector nozzle holes, as depicted in Fig. 1 – right. The proposed hybrid bowl has the same bore and squish

Table 1
Test engine main features.

Engine type	4-stroke, direct injection
Number of cylinders [–]	4
Number of Valves [–]	4
Displacement [l]	1.6
Compression ratio	16:1
Turbocharger	Single-Stage with Variable Geometry Turbine (VGT)
Fuel injection system	Common rail w/ max rail pressure 2000 bar
Maximum power	100 kW @ 4000 RPM
Maximum torque	320 Nm @ 2000 RPM

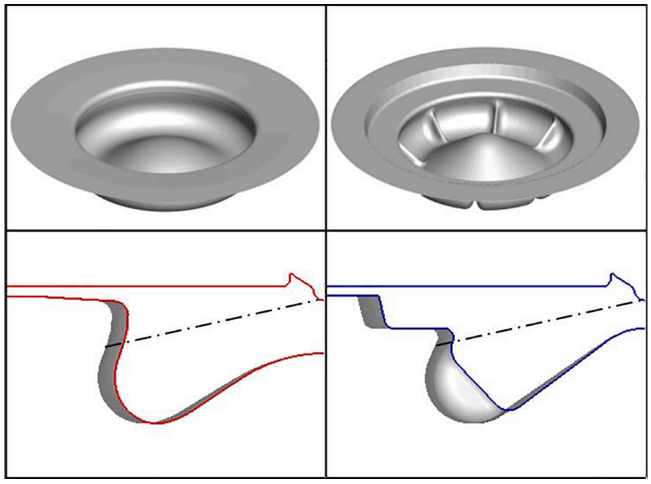

Fig. 1. Top: 3D – isometric view of the piston bowl geometries under investigation; bottom: 3D – vertical plane view of a single sector of the full cylinder geometry and the spray axis at TDC in dash-dot line. Left: re-entrant; right: hybrid. Image reproduced from [26]

height of the re-entrant bowl, while a reduced compression ratio (i.e., 15:1) is achieved. More specifically, Fig. 1 – top shows a 3D – isometric view of the piston bowl geometries under investigation. Fig. 1 – bottom shows a 3D – vertical plane view of a single sector of the full cylinder geometry and the spray axis at TDC in dash-dot line.

Lastly, a partial load engine operating condition (i.e., 1500 RPM × 4.6 bar of Indicative Mean Effective Pressure (IMEP)) was selected for the numerical simulations.

2.2. Simulation setup

The numerical simulations were carried out by means of the previously developed and validated 1D-/3D-CFD coupling methodology, widely discussed in [27]. The main steps of the methodology can be summarized as follow. Firstly, the 1D-CFD complete engine model built in GT-SUITE and validated in [28], provided the time-dependent boundary conditions at the intake and exhaust ports (i.e., thermodynamic state and species concentration). Then, the 3D-CFD simulation of the full cylinder engine was performed in CONVERGE CFD, assessing the gas exchange process evolution in terms of in-cylinder pressure, temperature and flow field without considering the combustion process. Afterwards, starting from the Intake Valve Closure (IVC), the compression stroke and the combustion process were simulated for a single sector of the complete cylinder geometry, centered with the spray axis. Finally, the 3D-CFD results were post-processed by means of GT-SUITE, providing consistency among experimental in-cylinder pressure analysis, 1D-CFD and 3D-CFD simulation results. As far as the 3D-CFD simulations are concerned, the Reynolds-averaged Navier-Stokes (RANS) based re-Normalization Group (RNG) k-ε model [29] was considered. The general settings in terms of mesh grid, turbulence and heat transfer models are summarized in Table 2, further details on the simulation setup are reported in [27].

The spray modelling was based on the 'blob' injection method [32] with a calibrated Kelvin-Helmholtz and Rayleigh-Taylor (KH-RT) breakup models [32]. The sub-models used for the spray modelling are listed in Table 3.

For the combustion modelling, the SAGE detailed chemistry was adopted, considering the Skeletal Zeuch reaction mechanism for *N*-Heptane oxidation (121 species, 593 reactions) [37]. The selected reaction scheme features both the NO_x reactions and the Poly-cyclic Aromatic Hydrocarbons (PAH) soot precursor chemistry, thus enabling the possibility to use the Particulate Mimic (PM) soot model for the soot mass prediction [38–40].

Table 2
Mesh grid, turbulence and heat transfer models.

Base grid / Minimum grid size	0.50 / 0.25 mm
Fixed embedding	Injector spray cone angle
Adaptive mesh refinement (AMR)	Velocity/temperature sub-grid criterion [30]
Turbulence model	RNG k-ε model
Heat transfer model	O'Rourke and Amsden [31]

3. Experimental methodology

3.1. Engine and test cell

The experimental tests were carried out in a single cylinder optical diesel engine which is based on the same 4-cylinder 1.6 L light-duty diesel engine previously described, based on the Bowditch design (detailed information about the engine can be found in [41]). It has 402 cm^3 displacement, where bore and stroke are the same as of the metal engine version and are summarized in Table 4. The original cylinder head of the metal engine, which is equipped with four valves per cylinder and a centrally located 8 holes injector, was also used in the optical engine. Moreover, to avoid the lateral optical accesses when the piston is at Top Dead Center (TDC), a lower position of the piston rings than with the conventional engine was used, thus resulting in lower compression ratio.

For the fuel injection, a conventional fuel pump and common rail system were employed. The management was done by a DRIVVEN® control unit, which allowed flexibility to configure the injection parameters. The optical access used for measurements is ensured through the piston bottom thanks to a fully transparent quartz piston. In this study, two different quartz bowls were used (re-entrant and hybrid), reproducing the bowl geometries under investigation, previously shown in Fig. 1. The hybrid design combined the annular recess step with radial protrusions in one half of the piston while the other half presented only the first feature, as shown in Fig. 2. To match the 3D-CFD design and avoid as much as possible the interaction among the different layouts, the analysis of the experimental results was restricted to the central region between two consecutive radial bumps (highlighted in red).

Regarding the test cell, the engine speed and load is controlled by a Schenck dynamometer (220 kW and 562 Nm). The intake air is pressurized by a screw compressor and before reaching the intake port it goes through a dryer and a heat exchanger [23]. The pressure pulses are avoided by the utilization of a settling chamber in the intake and exhaust lines. The target air temperature for each test is obtained by an air heater assembled inside the intake settling chamber. In addition, a back-pressure regulator is used to control the exhaust pressure. The instantaneous in-cylinder, intake and exhaust pressures were measured with piezoelectric transducers (AVL GH13P) connected to charge amplifier (Kistler 4603B10). A Yokogawa DL7008E oscilloscope recorded the instantaneous signals, synchronized by a shaft encoder.

The experimental tests were carried out at 1250 RPM and 4.5 bar IMEP. Four injections per cycle (pilot 1, pilot 2, main and post) at 670 bar were used. It was kept unchanged for both pistons, which led to an engine load of 4.5 bar IMEP in both cases. The fuel was injected 1 out of 20 cycles (skip-fire mode) to reduce the optical access fouling and to

Table 3
Spray sub-models.

Discharge coefficient model	Cv correlation [30]
Breakup model	Calibrated KH-RT
Turbulent dispersion	O'Rourke model [33]
Collision model	No Time Counter (NTC) collision [34]
Drop drag model	Dynamic drop drag [35]
Evaporation model	Frossling model [33]
Wall film model	O'Rourke [36]

Table 4
Optical engine characteristics.

Engine type	4-stroke, direct injection
Number of cylinders [–]	1
Number of Valves [–]	4
Bore [mm]	80
Stroke [mm]	80.1
Compression ratio [–]	12.5:1 (re-entrant) /11.5:1 (Hybrid)
Displacement [l]	0.402

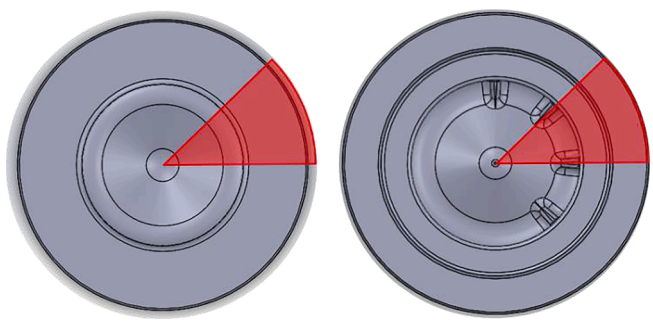

Fig. 2. Piston bowl geometries adopted for the optical engine. Left: re-entrant; right: hybrid. Image reproduced from [26]

prevent excessive thermal stress.

3.2. 2-Color pyrometry

The 2-color pyrometry technique (2C) is based on the use of thermal radiation at two different wavelengths to obtain the temperature and emissivity of the emitting source. The spectrum of thermal radiation emitted by a black body is described by the Planck's law:

$$I_{b,\lambda} = \frac{C_1}{\lambda^5\left[e^{\left(\frac{C_2}{\lambda \cdot T}\right)} - 1\right]} \tag{1}$$

where $I_{b,\lambda}$ represents the monochromatic intensity of radiation of a black body, $C_1 = 1.1910439 \cdot 10^{-16}$ W·m^2/sr and $C_2 = 1.4388 \cdot 10^{-2}$ m·k are the first and second Planck's constants, λ is the wavelength and T is the temperature of the emitting source. However, any real source has a lower intensity of radiation (I_λ) than a black body at the same temperature. To account for this, Eq. (1) is modified introducing its emissivity (ε) as follows:

$$I_\lambda = \varepsilon \cdot I_{b,\lambda} \tag{2}$$

For soot particles, their emissivity can be expressed by the Hottel and Broughton empirical correlation [42] that is represented by Eq. (3):

$$\varepsilon_{soot}(KL, \lambda) = 1 - e^{-(KL/\lambda^\alpha)} \tag{3}$$

where λ must be expressed in μm and α = 1.39 for most fuels within the visible range [43]. The KL parameter is the soot optical density and represents all the soot along the optical path of the flame. This parameter is directly related to the soot volume fraction. When soot radiation at two different wavelengths is measured, this set of equations can be applied to both of them, evaluating the soot temperature and KL. Whit this aim, the apparent temperature ($T_{a,\lambda}$) was introduced as the temperature of a blackbody that emits the same radiation intensity of a non-blackbody at a different temperature and at a given wavelength [44]. Then, the intensity of radiation measured at each wavelength ($I_{\lambda,meas}$) can be calculated as the radiation emitted by a blackbody at the corresponding $T_{a,\lambda}$, according to Eq. (4):

$$I_{\lambda,meas} = \frac{C_1}{\lambda^5\left(e^{\frac{C_2}{\lambda T_{a,\lambda}}} - 1\right)} \tag{4}$$

By substituting Eq. 1–3–4 into Eq. (2), the KL factor can be expressed by the following Eq. (5):

$$KL = -\ln\left\{1 - exp\left[-\frac{C_2}{\lambda}\left(\frac{1}{T_{a,\lambda}} - \frac{1}{T}\right)\right]\right\}^{\lambda^\alpha} \tag{5}$$

Being the KL independent of the wavelength, two equations with the same form, as Eq. (5), can be written to evaluate the temperature of the soot surface, as shown in Eq. (6):

$$\left\{1 - exp\left[-\frac{C_2}{\lambda_1}\left(\frac{1}{T_{a,\lambda_1}} - \frac{1}{T}\right)\right]\right\}^{\lambda_1{}^\alpha} = \left\{1 - exp\left[-\frac{C_2}{\lambda_2}\left(\frac{1}{T_{a,\lambda_2}} - \frac{1}{T}\right)\right]\right\}^{\lambda_2{}^\alpha} \tag{6}$$

Once determined the temperature T, the soot KL factor was evaluated from Eq. (5).

To measure radiation emitted by soot particles, two identical detection system were used. A representation of the optical set up can be found in Fig. 3. The visible flame radiation comes from the main optical access (piston bottom) and it is reflected by a 45° mirror towards the beam splitter mirror. This mirror divides the incident radiation by reflecting 50 % of it towards the detection system 1 and transmitting the other 50 % towards the detection system 2. Each system was composed of a high-speed CMOS camera (Photron SA-5), equipped with 100 mm focal length lens with f/2 aperture (Carl Zeiss Makro-Planar). To register only radiation at a specific wavelength, a 50 mm narrowband bandpass filter was placed in front of each lens. Their transmission band was centred at 550 and 660 nm respectively, with ±10 nm full width half maximum. The cameras were triggered through the start of energizing and both were synchronized between them to ensure the frame-to-frame correspondence, and, in both cases, the acquisition rate was set at 25.000 fps. However, a different exposure time was set for each detector to maximize the dynamic range used. Thus, 6.65 μs was set to register 660 nm radiation while 10.05 μs was utilized for the 550 nm radiation. The image size was 512 × 512 pixels, with 8.1 pixel/mm resolution. To transform the digital signal from the cameras into intensity of radiation, a tungsten-ribbon calibration lamp (Osram Wi17G) was used. Following the procedure described in [45], the calibration lamp was located on top of the piston (flat area) and its radiation was registered using the same optical set-up as the experiments (including all the optical elements).

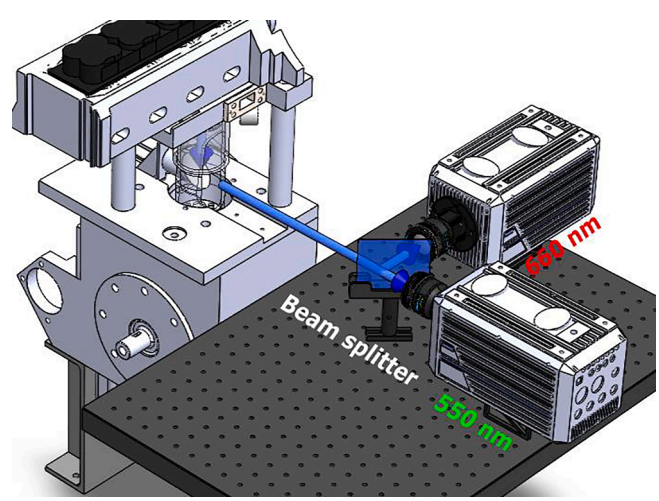

Fig. 3. Optical set-up.

4. Line-of-sight integration

In order to compare the numerical 3D soot distribution with the optical 2D soot density KL, a line-of-sight (LOS) integration methodology was employed. In this way, an interpretation of the third dimension along the optical depth was done, providing a bi-dimensional distribution also for the numerical results. Firstly, the product of soot volume fraction (f_v) and the LOS path length (L) was computed, representing a quantitative measure of soot along the optical depth [46]. Although this quantity can be easily computed, the experimental f_vL is not directly measured. Therefore, an additional methodology based on LOS integration was employed to obtain the numerical soot-KL distribution.

4.1. Soot volume fraction – f_vL

Thanks to the detailed kinetic mechanism and the PM soot model, the f_v distribution within the computational domain can be predicted. In order to obtain the f_vL planar distribution, the integration along the LOS was carried out following the Eq. (7) for each column of computational cells, as shown in Fig. 4. This integration results in a quantity directly related to soot along the LOS, while the optical soot density KL derives from a light integration where the soot transmissivity can have a significant influence [47].

$$(f_vL)_{i,j} = \sum_{k=1}^{N} (f_vL)_{i,j,k} \tag{7}$$

4.2. Optical soot density – KL

As previously mentioned, a line-of-sight integration of the numerical results was developed to provide an equivalent 2-color pyrometry methodology in the 3D-CFD environment, as shown in [47]. By computing the bi-dimensional distribution of the monochromatic intensity of radiation (I_λ) for the same wavelengths (λ) adopted in the experimental analysis (550 and 660 nm), the 2-color pyrometry algorithm was adopted to extract the numerical soot-KL. With this aim, the KL factor was computed for each cell of the computational domain following the Eq. (8), as suggested by Kamimoto et al. in [44]:

$$KL = 6\pi E(m) f_v L \tag{8}$$

where f_v and L are the soot volume fraction and the vertical length of each computational cell, respectively. E(m) is related to the complex refractive index of soot particles (m) that is a function of the wavelength, but it can be considered constant in the visible spectra range [44]. In this work a E(m) equal to 0.245 was adopted, as also reported in [47] for a similar investigation on an optical engine. Considering the temperature and the KL of each computational cell, the I_λ was evaluated by means of Eq. 1–2–3. Then, the line-of-sight integration of I_λ was evaluated for each column of cells as highlighted in Fig. 5, providing an interpretation

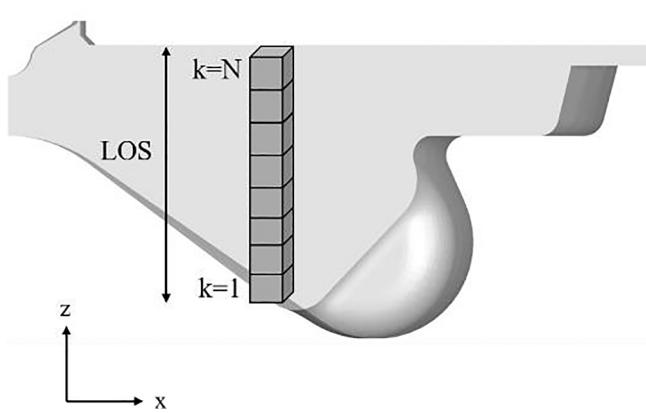

Fig. 4. LOS computational column.

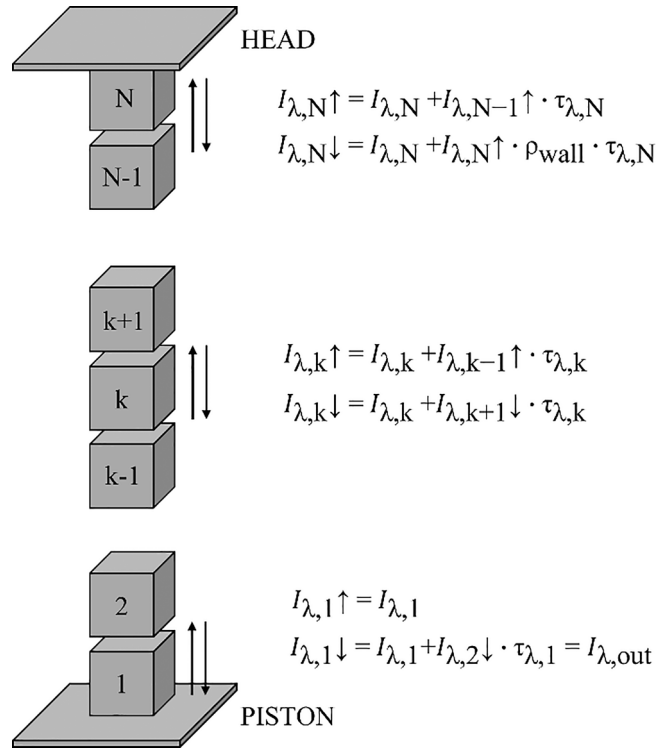

Fig. 5. Scheme and equations for LOS computation.

of the vertical direction (i.e., along the cylinder axis) and resulting into a bi-dimensional distribution of I_λ. In this analysis, each computational cell was assumed with homogeneous composition and only soot was involved in the light transfer process, while the surrounding gas was considered fully transparent [47]. In addition, only the radiation emitted along the vertical direction was considered in the computation, assuming that the detector was at a sufficient distance from the emitter [47]. In the radiation transfer process, only a part of the radiation emitted from soot passes through the domain in which it travels. The fraction of light transmitted was estimated by the soot transmissivity (τ_λ), following the Kirchhoff's law [48] and neglecting scattering, as the complement of the soot emissivity:

$$\tau_\lambda = 1 - \varepsilon_\lambda \tag{9}$$

The scheme and equations used in the line-of-sight integration technique are shown in Fig. 5. Considering the light reflection induced by the cylinder head, a set of equations was defined for the two vertical direction (i.e., upward – from the piston to the head, downward – form the head to the piston). The intensity of radiation emitted by the cell-k along the upward ($I_{\lambda,k}\uparrow$) or downward ($I_{\lambda,k}\downarrow$) directions can be expressed by the sum of two contributions: the radiation emitted by the cell itself ($I_{\lambda,k}$) and the radiation transmitted from the adjacent cell, which is affected by the soot transmissivity. Regarding the cell adjacent to the cylinder head, the radiation emitted in the upward direction is reflected by the wall surface with a certain reflectivity (ρ_{wall}). By integrating the equations firstly upward and then downward, $I_{\lambda,out}$ at the piston surface for the two selected wavelength was obtained. Then, following the 2-color pyrometry methodology previously described for the experimental analysis, the KL factor can be extracted even for the simulations.

5. Results and discussion

5.1. In-cylinder pressure and heat release rate

In order to investigate the piston bowl impact on the combustion

process, the numerical results were compared against the experimental data from the optical engine in terms of heat release rate, as shown in Fig. 6. The same IMEP was reached in both the simulations and experiments adopting similar injection strategy. It is worth to note that due to the intrinsic differences between the metal engine (in simulation) and the optical engine (in the experiments), only a qualitative comparison was carried out. Nevertheless, this was considered a fundamental step to assess the predictiveness of the developed numerical model and the methodology employed. Starting from the numerical results (Fig. 6 – left), similar combustion of the first pilot injection is shown for both the piston bowls during the free flame development. Moving toward the TDC, the combustion of the second pilot and main injections leads to lower HRR for the hybrid bowl. In this phase, in the flame-to-wall impingement area, the oxygen availability is reduced by the presence of the radial bumps wall, thus leading to lower mixing rate [20]. Moreover, at this stage, the hybrid bowl highlight a reduced swirling flow [26] which slightly affects the spray development, increasing the flame-to-wall interaction and thus reducing the combustion rate. Similar behaviour can be observed for the experimental HRR in Fig. 6 – right, confirming the predictive capabilities of the numerical models. Differently, after the EOI of main event, the hybrid bowl keeps a higher heat release intensity in comparison with the re-entrant bowl since the radial bumps mitigate the flame-to-flame interaction and enhance the mixing mechanisms towards the cylinder axis [26]. Again, a qualitative good agreement can be observed with respect to the experimental data, well capturing the timing when the phenomenon occurs. Nevertheless, the experiments showed a reduced difference between the designs under investigation. However, as already mentioned, this result was expected considering the different engine layout (metal vs optical engines) and the different operating conditions (e.g., initial thermodynamic conditions due to different compression ratio). After the EOI of post event, the re-entrant bowl highlights a more intense heat release with respect to the hybrid one due to the higher swirl ratio that increases the combustion rate of the residual fuel [26], as also experimentally confirmed in Fig. 6 – right.

5.2. Soot distribution

Once assessed the combustion results in terms of HRR, the soot analysis was carried out, considering the numerical methodologies previously described. The numerical soot distributions were compared with the experimental KL images, providing additional insights of the piston bowl effects on soot evolution, both in terms of formation and oxidation. The experimental optical analysis was focused only in a specific region of the bowl, within the radial bumps, as shown by the green area in Fig. 7. Indeed, the center of the bowl was excluded to avoid light reflections and distortions, while the squish zone was not considered due to the difficulty of isolating the impact of the bumps in this region. Similarly, the same region of interest was selected for the numerical analysis, as shown in Fig. 7 – left.

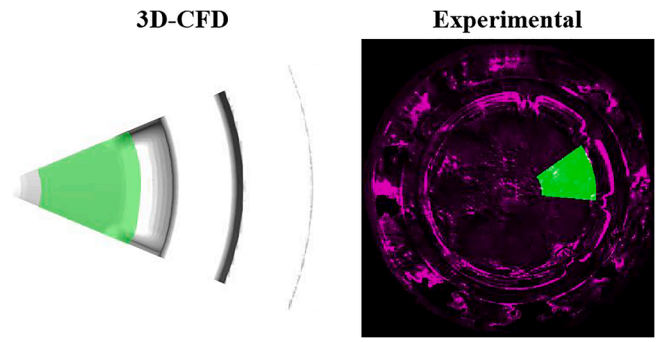

Fig. 7. Numerical and experimental investigation area.

In order to provide a global index of soot evolution, the average KL over the selected region was evaluated. With this aim the total amount of cells/pixels (A_a) for the numerical/experimental images was computed as reported in Eq. (10):

$$A_a = \sum_{i=cells,a} i \tag{10}$$

The sum of KL over the cells/pixels of the defined region provided the cumulative KL ($KL_{cumul,a}$), following Eq. (11):

$$KL_{cumul,a} = \sum_{i=cells,a} KL_i \tag{11}$$

Finally, the global average of KL factor over the defined region (KL_{mean}) was defined in Eq. (12):

$$KL_{mean} = \frac{KL_{\ cumul,a}}{A_a} \tag{12}$$

It is worth to note that only a qualitative comparison between the numerical and the experimental results was carried out by looking to the normalized results. Indeed, a different magnitude of the KL can be expected due to the intrinsic differences in terms of engine layout (i.e., metal engine in simulations vs optical engine in the experiments) and the different techniques adopted for the KL estimation (i.e., numerical methodology vs 2-colour pyrometry). Nevertheless, the qualitative comparison between the experiments and numerical results, each of them normalized with their corresponding maximum value, can be considered extremely important to identify the main phenomena that

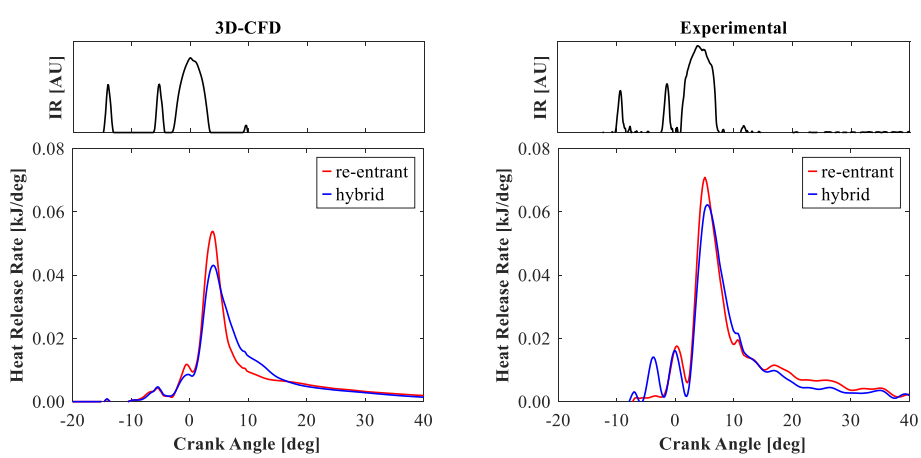

Fig. 6. Injection rate profile and Heat Release Rate. Left: 3D-CFD. Engine operating condition: 1500 RPM × 4.6 bar IMEP; right: experimental. Engine operating condition: 1250 RPM × 4.5 bar IMEP.

govern the soot formation/oxidation processes in innovative piston designs. Fig. 8 shows the normalized KL_{mean} over the defined region for each piston bowl design under investigation. Considering the numerical results (Fig. 8 – left), the re-entrant and hybrid bowls highlight similar soot formation rate up to +20 CAD aTDC. Then, the hybrid bowl results in lower peak of the KL factor with respect to the re-entrant bowl. Moving ahead in the cycle, the hybrid bowl highly attenuates KL, suggesting a strong impact of the hybrid bowl on the soot oxidation rate. As far as the experimental results are concerned (Fig. 8 – right), a qualitative good agreement with simulations can be observed. Even in this case, the hybrid bowl highlights a remarkable improvement of soot oxidation in the late phase, as shown by the KL mitigation. However, the time involved by the whole soot formation/oxidation process appears significantly reduced with respect to the numerical results. This could be related to the intrinsic differences between the metal and optical engines used in the numerical and experimental analysis, respectively. In addition, the soot PM model was validated against experimental engine-out soot emissions measured from the 4-cylinder metal engine [27]. Therefore, no calibration of the whole soot evolution (soot formation/oxidation rates) was performed. Nevertheless, the qualitative good agreement confirms on one side the predictive capabilities of the numerical methodology and on the other side, the radial bumps beneficial effects on soot evolution.

To further understand the potentials of the developed methodology to directly compare the numerical and the experimental results, the bidimensional distributions of the numerical f_vL and KL factors were assessed and compared with the optical soot density KL on the whole cylinder sector. Fig. 9 and Fig. 10 show these comparisons at four specific crank angle degrees, highlighted in Fig. 8, for the re-entrant and the hybrid bowls, respectively. More specifically, numerical f_vL factor and KL, normalized with respect to its maximum value, are depicted in the first and the second column, while the normalized experimental KL is reported in the last column.

At θ_1 – Initial soot formation phase

Similar results can be observed for the numerical f_vL and KL factors. Indeed, the reduced soot content (high transmissivity) does not introduce a significant light attenuation in the radiation transfer process along the line-of-sight. Therefore the f_vL value can be considered as a good index to be compared with the optical soot density KL, although it is based on a simplified approach. The comparison between the numerical distributions and the optical soot density KL shows a qualitative good agreement. In particular, the high magnitude region is confined on the piston bowl rim where the flame/wall interaction occurs. It is worth to note that the edge of the bowl leads to a significant light distortion and the experimental 2-color pyrometry results in false KL values. Therefore, the comparison with the numerical results should be considered only far enough from the piston surface. Focusing on the comparison between the re-entrant (Fig. 9) and the hybrid bowl (Fig. 10), no significant differences can be observed, as also confirmed by the global average KL highlighted in Fig. 8.

At θ_2 – Soot peak

Even in this timing, when the soot KL reaches its maximum values (see Fig. 8), no significant differences can be observed between the two proposed numerical methodologies. At this stage, the re-entrant bowl shows high magnitude soot near the bowl surface in both numerical results and experiments (Fig. 9). On the other side, the radial bumps in the hybrid bowl are able to mitigate the flame-to-flame interaction and thereby the soot formation in the collision area (Fig. 10). Additionally, the high magnitude soot is shifted toward the cylinder center, where the high oxygen content can improve the soot oxidation process. These results are in line with the optical analysis, however, in this latter a region with intense KL is highlighted above the step in the squish region, due to the retarded injection rate profile, thus a different split of the spray on the step (see Fig. 6).

At θ_3 – Soot oxidation phase

Moving ahead in the cycle, both the numerical results and experiments highlight a remarkable soot magnitude attenuation. Starting from the re-entrant design, a homogeneous soot distribution within the bowl volume can be pointed out for both quantities from simulation and optical images. The optical KL highlights a still significant soot cloud in the squish region (Fig. 9 – c), that is not detectable in the simulation. On the other side, the hybrid bowl shows a remarkable soot attenuation close to the cylinder axis, resulting in an overall soot intensity lower than the re-entrant geometry, especially thanks to the more intense reverse flow that drives a faster air/fuel mixing [26], as confirmed by the experimental optical images. As previously pointed out, also in this case, the experiments show a region in which the KL is high close to the periphery of the bowl.

At θ_4 – Late stage

Considering the late phase of the soot oxidation process, both the numerical results and the experimental optical images highlight a significant reduction of soot, almost zeroing the KL factor in the hybrid bowl volume, as shown in Fig. 8. However, as expected due to the lower in-cylinder temperature, the high-KL cloud in the squish region is still present, and it is not predicted by the numerical model. The re-entrant bowl shows a higher soot content compared with the hybrid design and this is located within the bowl.

Eventually, it is worth to point out that similar results can be achieved considering the numerical f_vL and KL factors. Therefore, f_vL can be used for a qualitatively comparison with the optical soot density KL.

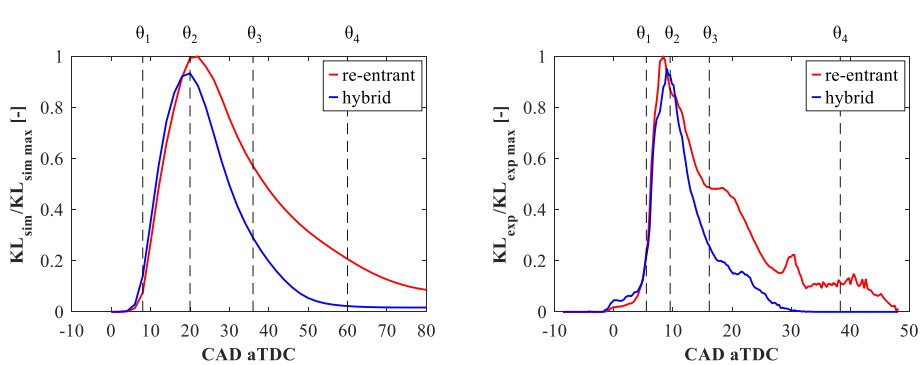

Fig. 8. Normalized KL_{mean} over the defined region. Left: 3D-CFD. Engine operating condition: 1500 RPM × 4.6 bar IMEP; right: experimental. Engine operating condition: 1250 RPM × 4.5 bar IMEP.

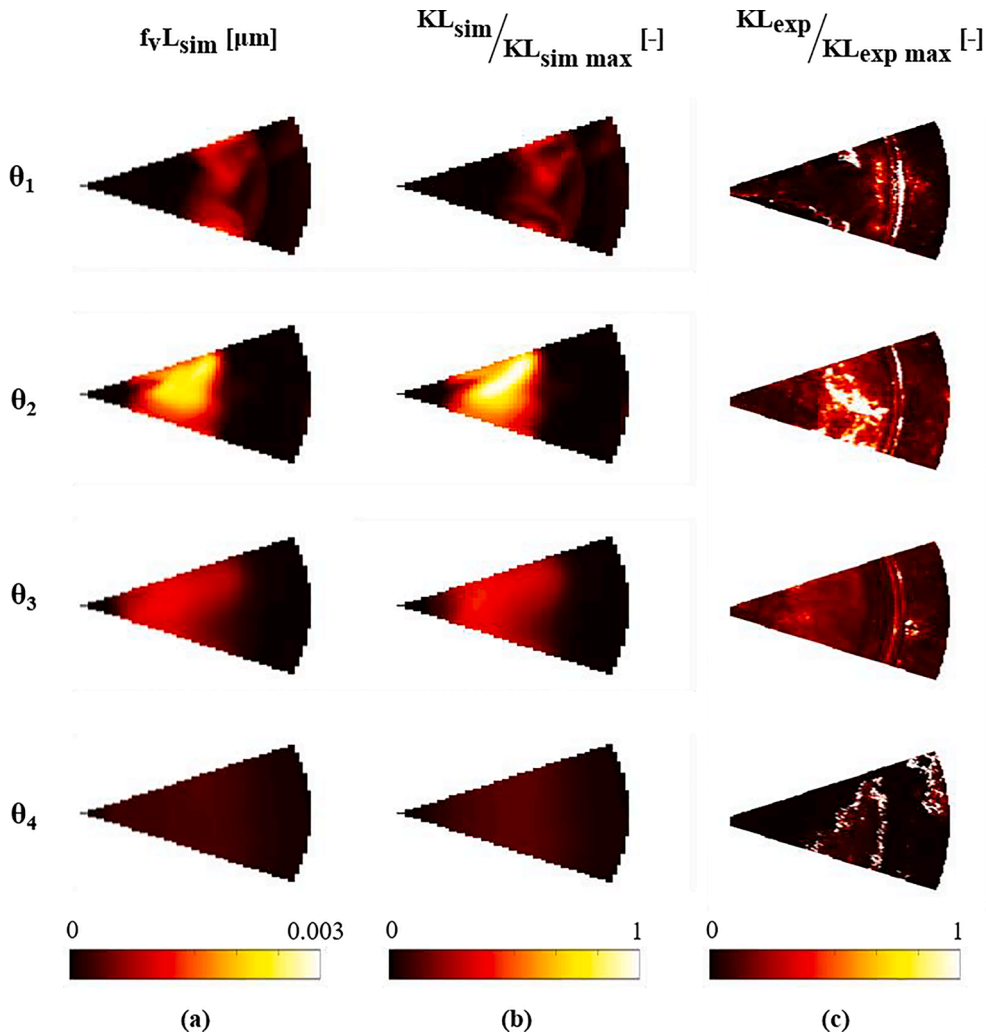

Fig. 9. Re-entrant bowl results. 3D-CFD $f_V L$ (a) and KL (b) normalized with respect to its maximum. Engine operating condition: 1500 RPM × 4.6 bar IMEP; (c) experimental KL normalized with respect to its maximum. Engine operating condition: 1250 RPM × 4.5 bar IMEP.

5.3. Temporal/spatial KL maps

5.3.1. Sector angle KL map

In order to further understand the piston bowl impact on soot distribution, a temporal and spatial soot KL map was developed. Starting from the experiments, the optical region of interest was divided in 5°-wide angular sectors in the azimuthal direction (φ) as shown in Fig. 11 – right, and the KL factor was averaged for each angular sector. Similarly, the numerical KL factor was averaged for each radial line, highlighted in Fig. 11 – left. The resulting average KL factor was defined in Eq. (13):

$$KL_{mean} = \frac{KL_{\ cumul,\ \varphi}}{A_{\varphi}} \tag{13}$$

where A_{φ} is the total amount of cells along the radial line/pixels in the angular sector, and $KL_{cumul,\varphi}$ is the cumulative KL for each radial line/angular sector.

Following this procedure, the average KL was defined in a 2D contour-map as shown in Fig. 12, where the evolution of the averaged KL factor as a function of the azimuthal direction (y-axis, in which 0 and 40 represent the radial bumps) and the crank angle (x-axis) is represented for the numerical (left) and experimental (right) analysis, each of them normalized respect to the corresponding maximum. As previously mentioned, the numerical and experimental soot KL evolution involve different time histories, therefore the soot KL evolutions on the 2D contour-map in Fig. 12 were investigated considering two different time intervals. In these latter, the soot evolution is quite similar, as already presented in Fig. 8 and reported in Fig. 12 – c for the sake of clarity.

Considering the re-entrant bowl (Fig. 12 – a), when the numerical KL factor reaches its maximum value, the KL contour map highlights the high magnitude region all around the sector angles. In particular, a more intense distribution can be observed near the sector periphery (0 and 40 sector angles), since the flames interaction in the collision zones increases the soot formation. This behaviour is observed even in the experimental map, but with different intensities. Moving ahead in the cycle, a still significant residual KL is detectable in the whole sector domain both for the numerical results and experiments. As far as the hybrid bowl is concerned (Fig. 12 – b), the KL magnitude in the sector periphery is remarkably reduced due to the presence of the radial bumps that mitigates the flame-to-flame interaction and consequently the soot formation. Moreover, the radial bumps drive the flame toward the sector center [26], where the high magnitude KL is highlighted. In this region, the more efficient soot oxidation process due to fresh oxygen availability leads to a more intense soot mitigation in comparison with the re-entrant bowl. Regarding the experimental map, similar results can be observed overall, however some discrepancies can be highlighted. In particular, a narrow high magnitude region is still present in the sector angle 0, but this is significantly attenuated ahead in the cycle with respect to the re-entrant bowl.

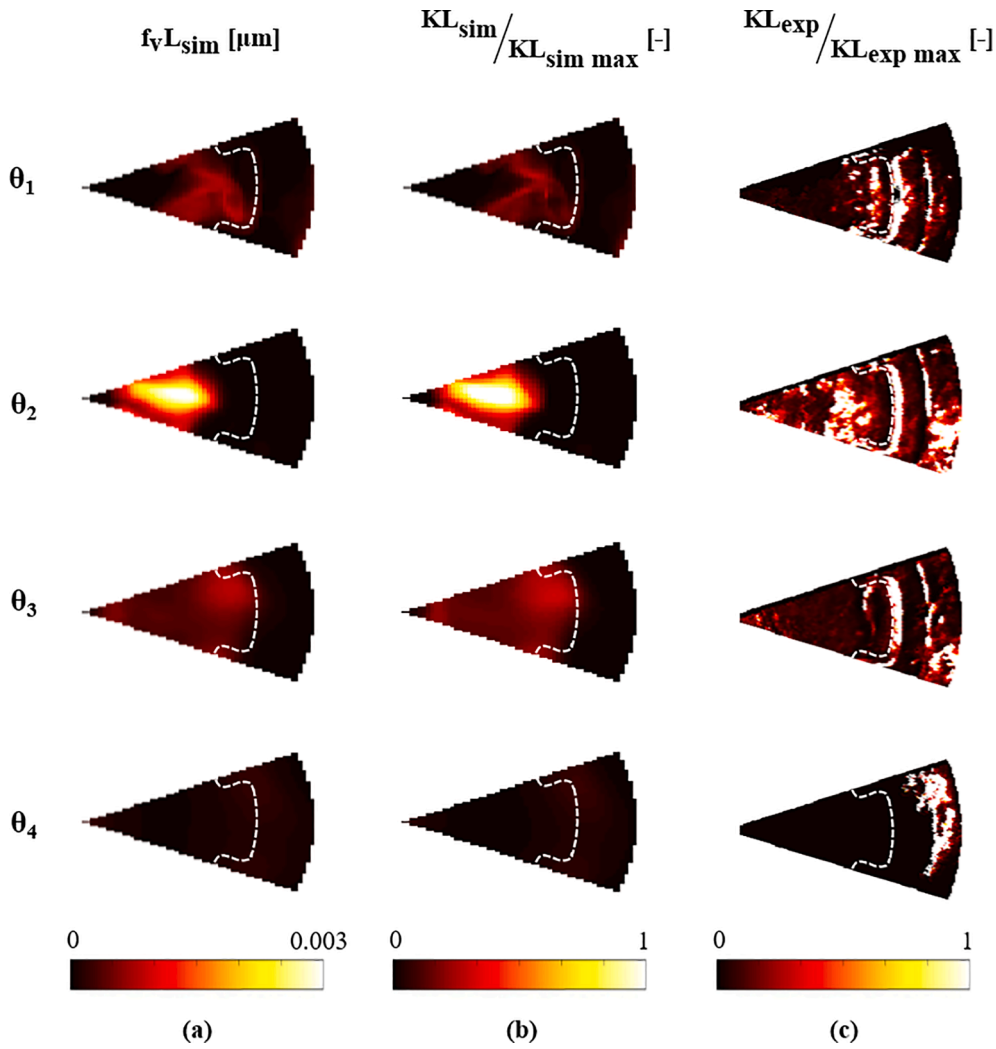

Fig. 10. Hybrid bowl results. 3D-CFD f_vL (a) and KL (b) normalized with respect to its maximum. Engine operating condition: 1500 RPM × 4.6 bar IMEP; (c) experimental KL normalized with respect to its maximum. Engine operating condition: 1250 RPM × 4.5 bar IMEP.

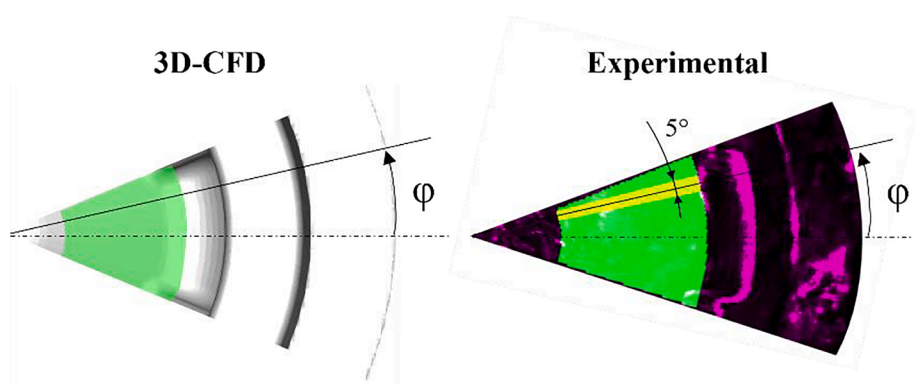

Fig. 11. 3D-CFD radial lines (left) and experimental sector angles (right) used for the average computation.

5.3.2. Radius KL map

Once assessed the average KL evolution along the azimuthal direction, a similar methodology was adopted to obtain a time and spatial evolution along the radial direction. With this aim, the optical region of interest was divided in rings with a thickness equal to 0.5 mm, as highlighted in Fig. 13 – right. Then, the KL factor was averaged for each ring, to provide an index of soot distribution along the radial direction (r). Similarly, the numerical KL factor was averaged for each arc showed in Fig. 13 – left. The resulting average KL factor was computed by following Eq. (14):

$$KL_{mean} = \frac{KL_{\ cumul,r}}{A_r} \tag{14}$$

where A_r is the total amount of cells along the arc/pixels in the ring, and $KL_{cumul,r}$ is the cumulative KL for each arc/ring.

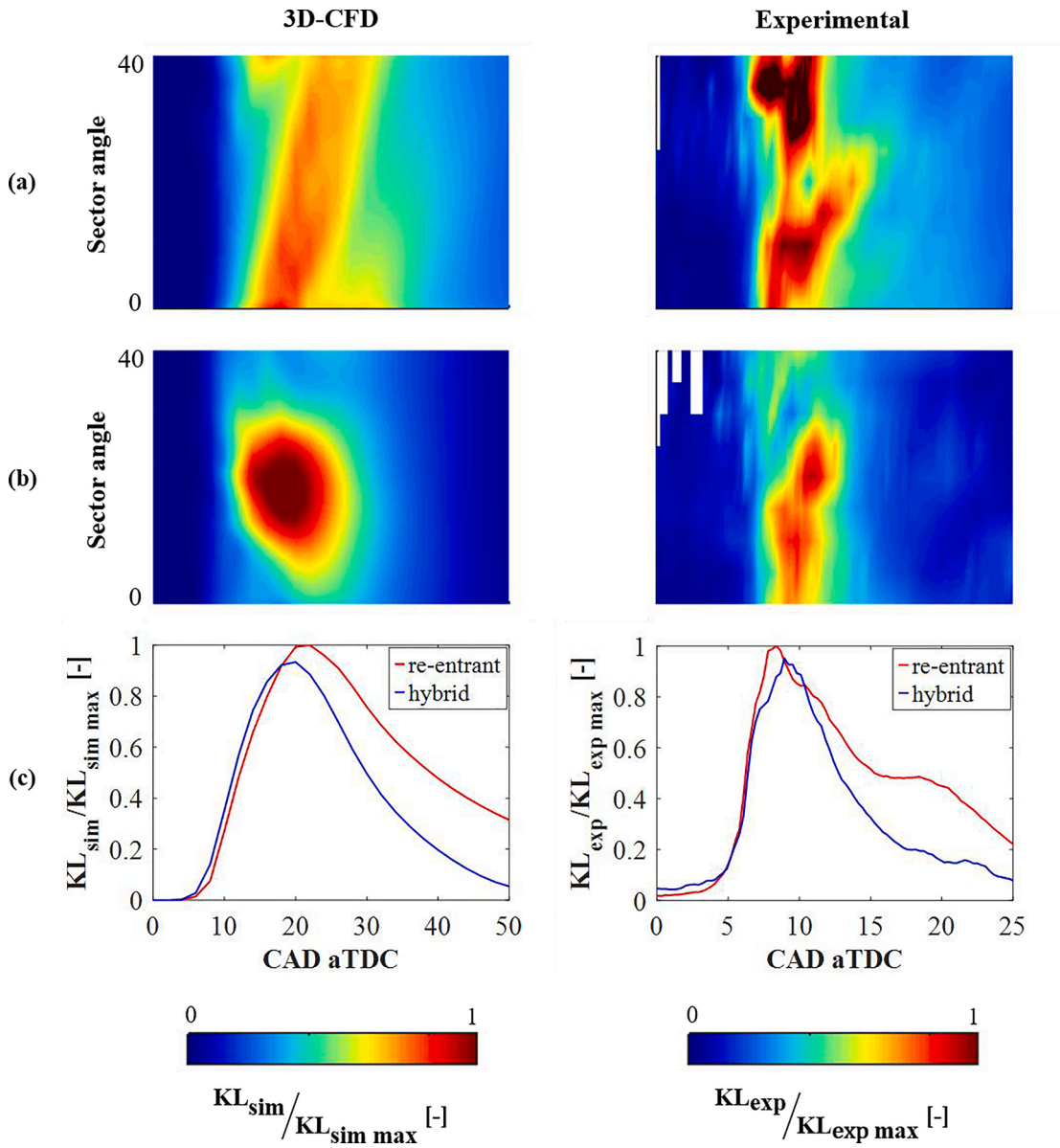

Fig. 12. Numerical (left) and experimental (right) sector angle KL maps. (a) re-entrant bowl; (b) hybrid bowl; (c) normalized KL_{mean}.

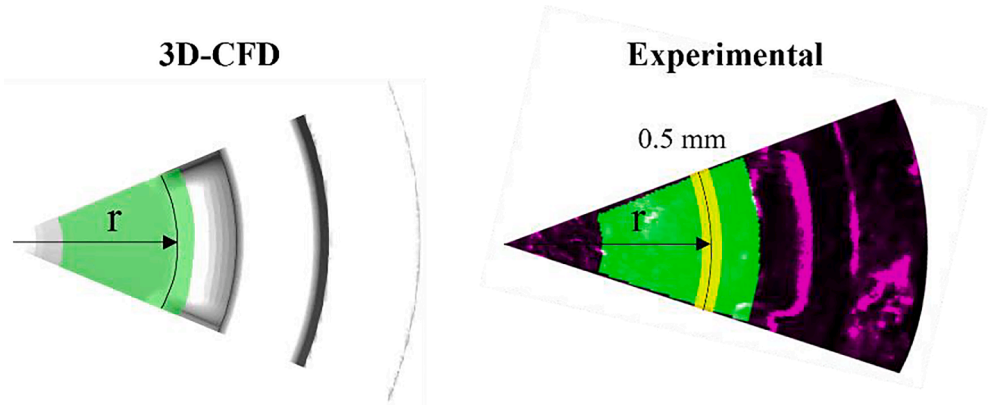

Fig. 13. 3D-CFD arcs (left) and experimental rings (right) used for the average computation.

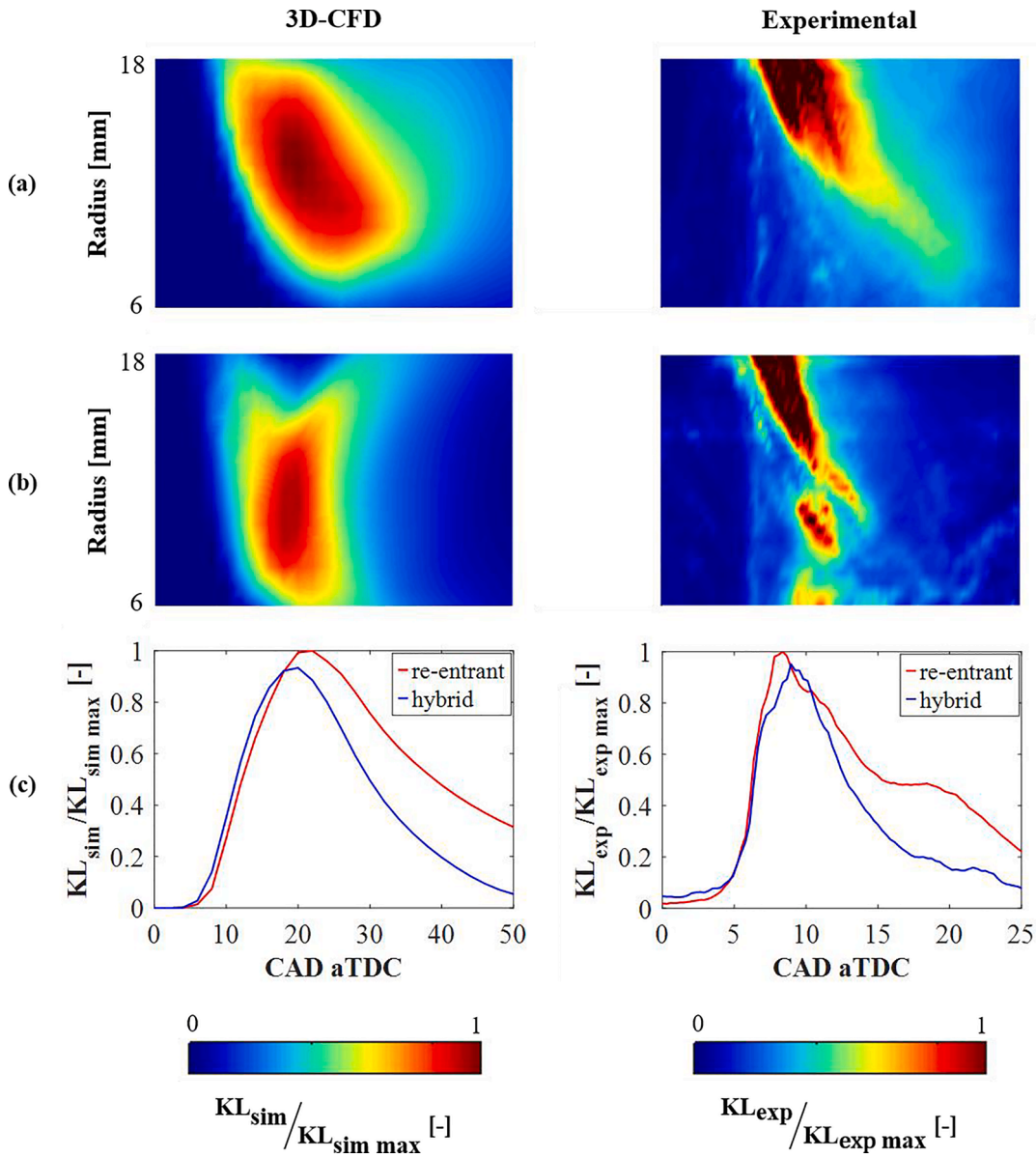

Fig. 14. Numerical (left) and experimental (right) radius KL maps. (a) re-entrant bowl; (b) hybrid bowl; (c) normalized KL_{mean}.

Thanks to this procedure, the evolution of the normalized averaged KL as a function of the radius (y-axis) and the crank angle (x-axis) can be depicted in a 2D contour-map for both simulations (left) and experiments (right), as shown in Fig. 14. As already carried out for the soot angular distribution in Fig. 12, even these maps were investigated considering two different time intervals to have comparable soot evolution, as shown in Fig. 14 – c.

The numerical KL distribution of the re-entrant design in Fig. 14 – a, shows that the high magnitude region starts to appear near the bowl surface (radius: 18 mm) due to the flame/wall interaction. Then, moving ahead in the combustion process the flame propagates toward the cylinder center due to the flame movement, reaching the radius 6 mm at +30 CAD aTDC. Moving to the experimental map, a qualitative good agreement can be observed for the KL distribution. Even in this case, a high magnitude region starts to appear near the bowl surface and then propagates toward cylinder center. However, a more intense attenuation is highlighted with respect to the numerical results, resulting in lower KL magnitude near the bowl center. This could be related to the retarded injection rate for the experiments that provides a different fuel distribution and thereby a reduced fuel amount within the bowl. Considering the hybrid bowl (Fig. 14 – b), the numerical map highlights a reduction of KL near the bowl surface during the first stages of the soot formation process. Instead, the flame is shifted toward the cylinder center (lower radius) thanks to the radial bumps which increase the flame velocity in the reverse flow [26]. Consequently, the flame reaches the radius 6 mm faster than the re-entrant bowl, at +15 CAD aTDC. This behaviour results in a remarkable improvement of the soot oxidation process, as confirmed by the strong attenuation of the KL intensity in the late cycle in comparison with the re-entrant bowl. The faster flame propagation toward the cylinder center can be also highlighted in the experimental map. Nevertheless, some differences are visible with respect to the numerical results. Indeed, on one hand, a more intense KL region is present near the bowl surface, while, on the other hand, the region near the radius 6 mm shows a lower intensity. As already mentioned, this effect could be mainly related to the retarded injection schedule which leads to different fuel split on the step, affecting the soot evolution within bowl.

6. Conclusions

The present study aims to analyse the potential soot reduction

derived from the adoption of an innovative hybrid bowl by means of both numerical simulations and experiments from an optical access engine. The innovative bowl design features both a highly-reentrant sharp-stepped bowl and radial bumps in the inner bowl rim. As far as experimental analysis is concerned, the 2-color pyrometry technique was adopted to obtain the optical soot density KL. Therefore, to directly compare the numerical soot distribution with the optical KL, two different methodologies were adopted. Firstly, the product of the soot volume fraction and the line-of-sight path length (f_vL) was computed to quantify soot along the optical depth. Nevertheless, the experimental f_vL is not directly measurable from the optical soot density KL, which instead derives from a light integration where soot transmissivity plays a significant role. For this reason, a line-of-sight integration of the numerical results was carried out to provide an equivalent 2-color pyrometry methodology in the 3D-CFD environment.

Following the abovementioned methodologies, the main outcomes of the activity can be summarized as follow:

- The numerical KL_{mean} over the region of interest highlighted a reduced soot formation rate for the hybrid bowl, leading to lower maximum value with respect to the re-entrant bowl. Moving ahead in the soot oxidation process, the hybrid bowl highlighted a strong KL_{mean} attenuation, confirming the crucial role of radial bumps on soot mitigation. This result highlighted a qualitative good agreement with the KL_{mean} obtained by the optical 2-color pyrometry technique.
- The numerical bi-dimensional distribution of f_vL and KL factors showed comparable results for both the bowls under investigation. Therefore, the soot content for this operating condition did not introduce a significant light attenuation in the radiation transfer process along the optical path length and the f_vL factor can be considered a good tracer to be compared with the optical KL.
- The comparison between the numerical distributions and the optical soot density KL showed a qualitative good agreement over the entire soot formation/oxidation processes, confirming the high predictiveness of the developed numerical methodologies. In particular, the hybrid bowl highlighted a reduced soot formation in the collision area of two adjacent flames thanks to the radial bumps. Then, the high magnitude soot region was shifted toward the cylinder center thanks to the faster reverse flow toward the cylinder center. This resulted in a more intense soot oxidation rate with respect to the re-entrant bowl.
- The temporal-spatial map of the average KL along the azimuthal direction confirmed the effect of the radial bumps on reducing the soot formation in the flame collision area during the whole combustion process. Moreover, the temporal-spatial map of the average KL along the radial direction highlighted for the hybrid bowl a faster flame velocity during the reverse flow which led to a significant KL attenuation in the late cycle. The hybrid bowl effects on soot formation/oxidation processes were also shown in the experimental KL maps, suggesting once again the reliability of the developed models.

The geometrical features of the hybrid bowl design highlighted great potentials for engine-out soot emissions reduction. Additionally, the line-of-sight numerical methodologies provided a reliable tool to directly compare the numerical soot results with the 2-color pyrometry optical data, allowing the qualitative assessment of the main trends that govern the in-cylinder soot evolution. Future analysis will be focused on additional piston design optimization enabled by the Additive-Manufacturing techniques, guaranteeing extremely complex geometry and the durability requirements for a diesel engine application.

CRediT authorship contribution statement

A. Piano: Methodology, Investigation, Writing – original draft, Writing – review & editing. **S. Roggio:** Investigation, Methodology, Writing – original draft. **F. Millo:** Conceptualization, Supervision, Project administration, Funding acquisition. **A. García:** Conceptualization, Supervision, Project administration, Funding acquisition. **C. Micó:** Methodology, Investigation, Writing – original draft, Writing – review & editing. **F. Lewiski:** Investigation, Methodology, Writing - original draft. **F.C. Pesce:** Conceptualization, Supervision, Project administration. **A. Vassallo:** Conceptualization, Supervision, Project administration. **A. Bianco:** Methodology, Investigation.

Declaration of Competing Interest

The authors declare that they have no known competing financial interests or personal relationships that could have appeared to influence the work reported in this paper.

Data availability

The data that has been used is confidential.

References

[1] Serrano JR, García A, Monsalve-Serrano J, Martínez-Boggio S. High efficiency two stroke opposed piston engine for plug-in hybrid electric vehicle applications: evaluation under homologation and real driving conditions. Appl Energy 2021; 282:116078. https://doi.org/10.1016/j.apenergy.2020.116078.

[2] Millo F, Piano A, Peiretti Paradisi B, Postrioti L, Pieracci L, Bianco A, et al. Ducted Fuel Injection: experimental and numerical investigation on fuel spray characteristics, air/fuel mixing and soot mitigation potential. Fuel 2021;289: 119835. https://doi.org/10.1016/j.fuel.2020.119835.

[3] Doppalapudi AT, Azad AK, Khan MMK. Combustion chamber modifications to improve diesel engine performance and reduce emissions: A review. Renew Sustain Energy Rev 2021;152:111683. https://doi.org/10.1016/j.rser.2021.111683.

[4] Pélerin D, Gaukel K, Härtl M, Jacob E, Wachtmeister G. Potentials to simplify the engine system using the alternative diesel fuels oxymethylene ether OME 1 and OME 3–6 on a heavy-duty engine. Fuel 2020;259:116231. https://doi.org/10.1016/j.fuel.2019.116231.

[5] García A, Gil A, Monsalve-Serrano J, Sari RL. OMEx-diesel blends as high reactivity fuel for ultra-low NOx and soot emissions in the dual-mode dual-fuel combustion strategy. Fuel 2020;275:117898. https://doi.org/10.1016/j.fuel.2020.117898.

[6] Pastor JV, García A, Micó C, Lewiski F. Simultaneous high-speed spectroscopy and 2-color pyrometry analysis in an optical compression ignition engine fueled with OMEX-diesel blends. Combust Flame 2021;230:111437. https://doi.org/10.1016/j.combustflame.2021.111437.

[7] Pastor JV, García A, Micó C, Lewiski F. An optical investigation of Fischer-Tropsch diesel and Oxymethylene dimethyl ether impact on combustion process for CI engines. Appl Energy 2020;260:114238. https://doi.org/10.1016/j.apenergy.2019.114238.

[8] Novella R, Bracho G, Gomez-Soriano J, Fernandes CS, Lucchini T. Combustion system optimization for the integration of e-fuels (Oxymethylene Ether) in compression ignition engines. Fuel 2021;305:121580. https://doi.org/10.1016/j.fuel.2021.121580.

[9] Eismark J, Christensen M, Andersson M, Karlsson A, Denbratt I. Role of fuel properties and piston shape in influencing soot oxidation in heavy-duty low swirl diesel engine combustion. Fuel 2019;254:115568. https://doi.org/10.1016/j.fuel.2019.05.151.

[10] Khan S, Panua R, Bose PK. The impact of combustion chamber configuration on combustion and emissions of a single cylinder diesel engine fuelled with soybean methyl ester blends with diesel. Renewable Energy 2019;143:335–51. https://doi.org/10.1016/j.renene.2019.04.162.

[11] Zha K, Busch S, Warey A, Peterson R, et al. A study of piston geometry effects on late-stage combustion in a light-duty optical diesel engine using combustion image velocimetry. SAE Int J Engines 2018;11(6):783–804. https://doi.org/10.4271/2018-01-0230.

[12] Busch S, Zha K, Kurtz E, Warey A. et al., Experimental and Numerical studies of bowl geometry impacts on thermal efficiency in a light-duty diesel engine, SAE Technical Paper 2018-01-0228, 2018, 10.4271/2018-01-0228.

[13] Busch S, Zha K, Perini F, Reitz R et al., Bowl Geometry Effects on Turbulent Flow Structure in a Direct Injection Diesel Engine, SAE Technical Paper 2018-01-1794, 2018, 10.4271/2018-01-1794.

[14] Neely G, Sasaki S, Sono H, Investigation of Alternative Combustion Crossing Stoichiometric Air Fuel Ratio for Clean Diesels, SAE Technical Paper 2007-01-1840, 2007, 10.4271/2007-01-1840.

[15] Smith A., Ricardo low emissions combustion technology helps JCB create the off-highway industry's cleanest engine, *Ricardo Press Release*, 2010, https://ricardo.com/news-and-media/news-and-press/ricardo-low-emissions-combustion-technology-helps.

[16] Cornwell R, Conicella F. Direct Injection Diesel Engines, Ricardo UK Limited, West Sussex (GB), U.S. Patent 8770168 B2, 2014.

[17] Dahlstrom J, Andersson O, Tuner M, Persson H. Experimental comparison of heat losses in stepped-bowl and re-entrant combustion chambers in a light duty diesel engine, SAE Technical Paper 2016-01-0732, 2016, 10.4271/2016-01-0732.

[18] Eder T, Kemmner M, Lückert P, Sass H. OM 654 – launch of a new engine family by Mercedes-Benz. MTZ Worldwide 2016.
[19] Zhang T, Eismark J, Munch K, Denbratt I. Effects of a wave-shaped piston bowl geometry on the performance of heavy duty Diesel engines fueled with alcohols and biodiesel blends. Renewable Energy 2020;148:512–22. https://doi.org/10.1016/j.renene.2019.10.057.
[20] Eismark J, Andersson M, Christensen M, Karlsson A, et al. Role of piston bowl shape to enhance late-cycle soot oxidation in low-swirl diesel combustion. SAE Int J Engines 2019;12(3):233–49. https://doi.org/10.4271/03-12-03-0017.
[21] Millo F, Piano A, Roggio S, Bianco A, et al. Numerical investigation on mixture formation and combustion process of innovative piston bowl geometries in a swirl-supported light-duty diesel engine. SAE Int J Engines 2021;14(2):247–62. https://doi.org/10.4271/03-14-02-0015.
[22] Millo F, Piano A, Roggio S, Bianco A. et al., Numerical assessment of additive manufacturing-enabled innovative piston bowl design for a light-duty diesel engine achieving ultra-low engine-out soot emissions, SAE Int. J. Engines 15(3):2022, 10.4271/03-15-03-0022.
[23] Pastor JV, García A, Micó C, Lewiski F. Soot reduction for cleaner Compression Ignition Engines through innovative bowl templates. Int J Engine Res 2020;1–15. https://doi.org/10.1177/1468087420951324.
[24] Belgiorno G, Boscolo A, Dileo G, Numidi F, et al. Experimental study of additive-manufacturing-enabled innovative diesel combustion bowl features for achieving ultra-low emissions and high efficiency. SAE Int J Adv & Curr Prac in Mobility 2021;3(1):672–84. https://doi.org/10.4271/2020-37-0003.
[25] Pastor JV, García A, Micó C, Lewiski F, et al. Effect of a novel piston geometry on the combustion process of a light-duty compression ignition engine: an optical analysis. Energy 2021;221:119764. https://doi.org/10.1016/j.energy.2021.119764.
[26] Millo F, Piano A, Roggio S, Pastor JV, et al. Mixture formation and combustion process analysis of an innovative diesel piston bowl design through the synergetic application of numerical and optical techniques. Fuel 2022;309:122144. https://doi.org/10.1016/j.fuel.2021.122144.
[27] Millo F, Piano A, Peiretti Paradisi B, Marzano MR, et al. Development and assessment of an integrated 1D–3D CFD codes coupling methodology for diesel engine combustion simulation and optimization. Energies 2020;13:1612. https://doi.org/10.3390/en13071612.
[28] Piano A, Millo F, Boccardo G, Rafigh M. et al., Assessment of the Predictive capabilities of a combustion model for a modern common rail automotive diesel engine, SAE Technical Paper 2016-01-0547, 2016, 10.4271/2016-01-0547.
[29] Orszag SA, Yakhot V, Flannery WS, Boysan F, et al. Renormalization group modeling and turbulence simulations. Near-Wall Turbulent Flows 1993;13:1031–46.
[30] Richards KJ, Senecal PK, Pomraning E. Converge 2.3 Manual. Madison, WI, USA: Convergent Science Inc.; 2016.
[31] Amsden AA, KIVA-3V: A Block Structured KIVA Program for Engines with Vertical or Canted Valves, Los Alamos National Laboratory Technical Report LA-13313-MS, 1997.
[32] Reitz RD, Bracco FV. Mechanisms of Breakup of Round Liquid Jets, *Encyclopedia of Fluid Mechanism*, 1986, 3, 233–249.
[33] Amsden AA, O'Rourke PJ, Butler TD, KIVA-II: A Computer Program for Chemically Reactive Flows with Sprays, Los Alamos National Laboratory Technical Report LA-11560-MS, 1989.
[34] Schmidt DP, Rutland CJ. A new droplet collision algorithm, *J Comput Phys*, 164 (1), 2000, 62–80, ISSN 0021-9991, 10.1006/jcph.2000.6568.
[35] O'Rourke P, Amsden A. The Tab Method for Numerical Calculation of Spray Droplet Breakup, SAE Technical Paper 872089, 1987, 10.4271/872089.
[36] O'Rourke P, Amsden A. A Spray/Wall Interaction Submodel for the KIVA-3 Wall Film Model, SAE Technical Paper 2000-01-0271, 2000, 10.4271/2000-01-0271.
[37] Zeuch T, Moréac G, Ahmed SS, Mauss F. A comprehensive skeletal mechanism for the oxidation of n-heptane generated by chemistry-guided reduction, *Comb Flame*, 155 (4), 2008, 651–674, ISSN 0010-2180, 10.1016/j.combustflame.2008.05.007.
[38] Frenklach, M. and Wang, H., "Detailed Modeling of Soot Particle Nucleation and Growth," *Symposium (International) on Combustion*, Volume 23, Issue 1, 1991, Pages 1559-1566, ISSN 0082-0784, 10.1016/S0082-0784(06)80426-1.
[39] Kazakov A, Wang H, Frenklach M. Detailed modeling of soot formation in laminar premixed ethylene flames at a pressure of 10 bar, *Comb Flame*, 100 (1–2), 1995, 111–120, ISSN 0010-2180, 10.1016/0010-2180(94)00086-8.
[40] Kazakov A, Frenklach M., Dynamic modeling of soot particle coagulation and aggregation: implementation with the method of moments and application to high-pressure laminar premixed flames, *Combust Flame*, 114 (3–4), 1998, 484-501, ISSN 0010-2180, 10.1016/S0010-2180(97)00322-2.
[41] Pastor JV, Olmeda P, Martín J, Lewiski F. Methodology for optical engine characterization by means of the combination of experimental and modeling techniques. Appl Sci 2018;8(12):2571. https://doi.org/10.3390/app8122571.
[42] Hottel HC, Broughton FP. Determination of true temperature and total radiation from luminous gas flames. Ind Eng Chem Anal Ed 1932;4(2):166–75. https://doi.org/10.1021/ac50078a004.
[43] Yan J, Borman G. Analysis and in-cylinder measurement of particulate radiant emissions and temperature in a direct injection diesel engine, SAE Technical Paper 881315, 1988, 10.4271/881315.
[44] Kamimoto T, Murayama Y. Re-examination of the emissivity of diesel flames. Int J Engine Res 2011;12(6):580–600. https://doi.org/10.1177/1468087411418170.
[45] Pastor JV, García-Oliver JM, García A, Micó C, Möller S. Application of optical diagnostics to the quantification of soot in n-alkane flames under diesel conditions. Combust Flame 2016;164:212–23. https://doi.org/10.1016/j.combustflame.2015.11.018.
[46] Hessel R, Yue Z, Reitz R, Musculus M, et al. Guidelines for interpreting soot luminosity imaging. SAE Int J Engines 2017;10(3):1174–92. https://doi.org/10.4271/2017-01-0716.
[47] Yu X, Zha K, Florea R, Jansons M. Comparison of in-cylinder soot evolution in an optically accessible engine fueled with JP-8 and ULSD. SAE Int J Fuels Lubr 2012;5(2):875–91. https://doi.org/10.4271/2012-01-1315.
[48] Modest MF. Radiative Heat Transfer, 2013, ISBN 9780123869449, 10.1016/B978-0-12-386944-9.50038-8.